

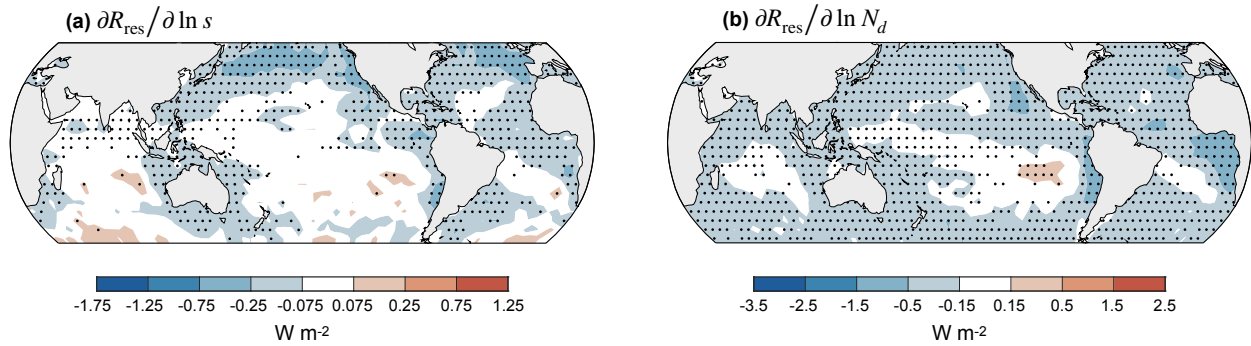
Supplementary Information

Global Observations of Aerosol Indirect Effects from Marine Liquid Clouds

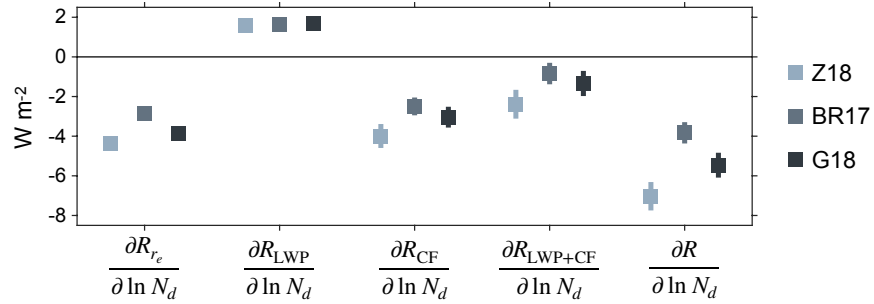
Contents of this file:

- Supplementary Figures 1-3
- Supplementary Tables 1-2
- Supplementary Text
- Supplementary References

1 **Supplementary Figures**

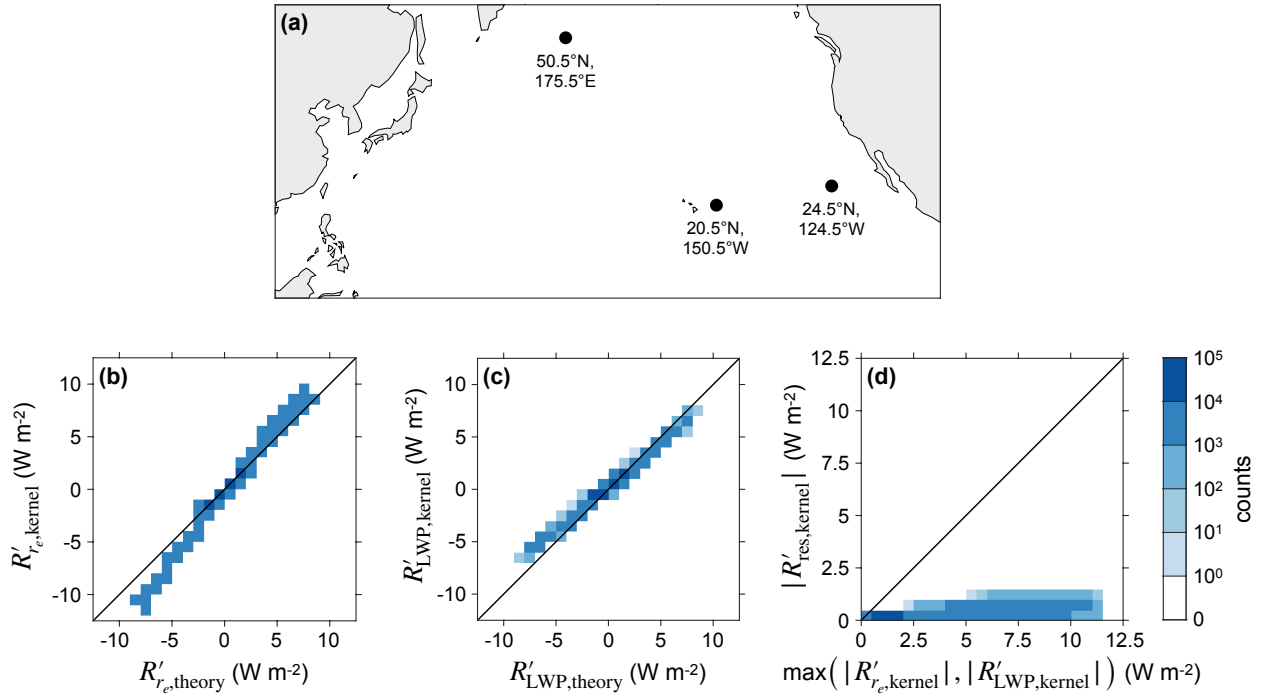


Supplementary Fig. 1 Relationships between the residual of the R decomposition (R_{res}) and local anomalies of two indicators of CCN concentration near cloud base. The CCN indicators include sulfate aerosol mass concentration at 910 hPa (s) and cloud droplet number concentration from cloudy pixels with the largest 10% optical thickness (N_d). Linear regression coefficients are plotted for (a) $\partial R_{\text{res}} / \partial \ln s$ and (b) $\partial R_{\text{res}} / \partial \ln N_d$. Stippling indicates regression coefficients that are significantly different from zero with the false discovery rate limited to 0.1 (Wilks, 2016). The averages of $\partial R_{\text{res}} / \partial \ln s$ and $\partial R_{\text{res}} / \partial \ln N_d$ over ocean between 55°S and 55°N are $-0.08 \pm 0.01 \text{ W m}^{-2}$ and $-0.26 \pm 0.01 \text{ W m}^{-2}$, respectively (95% CIs). Note that the contour values are one order of magnitude smaller than those in Fig. 2 of the main text.



15
16
17
18
19
20
21
22

Supplementary Fig. 2 Sensitivity test showing how the spatial average of $\partial R / \partial \ln N_d$ depends on the retrieval method for N_d . The Z18, BR17, and G18 cases retrieve N_d using filtering methods recommended by Zhu et al. (2018), Bennartz and Rausch (2017), and Grosvenor et al. (2018), respectively. These filtering methods select N_d in different subsets of liquid-cloud pixels. The Z18 case is presented in the main text. Squares show mean values, and vertical lines show 95% CIs.



23
24
25
26
27
28
29
30
31
32
33

Supplementary Fig. 3 Validation of the R' decomposition using synthetic-data test cases. (a) Locations of the $1^\circ \times 1^\circ$ grid boxes used in the test cases. The center of the grid box is labeled on the map. (b) Joint histogram showing the kernel-based estimate of R'_{r_e} plotted as a function of the theoretical estimate of R'_{r_e} . Each data point in the histogram represents one test case. (c) Similar to (b), but for R'_{LWP} . (d) Joint histogram showing the magnitude of the residual of the decomposition, $|R'_{res}|$, plotted as function of the maximum of $|R'_{r_e}|$ and $|R'_{LWP}|$. Values in (d) are computed using the kernel method. The color scale is logarithmic, and the bin spacing is 1 W m^{-2} in (b-c) and 0.5 W m^{-2} in (d).

34 **Supplementary Tables**

35
 36 **Supplementary Table 1** List of GCMs used in the study. CMIP6 output is used to
 37 compute $\Delta \ln s$, and CMIP5 and AeroCom output is used to compute the GCM estimates
 38 of ERFaci in Fig. 5 of the main text. CMIP6 and CMIP5 models are listed according to
 39 their Source ID on the CMIP online archives (<https://esgf-node.llnl.gov/projects/cmip6/>;
 40 <https://esgf-node.llnl.gov/projects/cmip5/>), and AeroCom models are listed according to
 41 the naming convention of Gryspeerdt et al. (2020).
 42

CMIP6 Models	CMIP5 Models	AeroCom Models
BCC-ESM1	CanESM2	ECHAM6-HAM2.2
CESM2	HadGEM2-A	HadGEM3-UKCA
CESM2-FV2	IPSL-CM5A-LR	CAM5.3
CESM2-WACCM	MIROC5	CAM5.3-MG2
CESM2-WACCM-FV2	MRI-CGCM3	CAM5.3-CLUBB
CNRM-ESM2-1		CAM5.3-CLUBB-MG2
EC-Earth3-AerChem		SPRINTARS
GISS-E2-1-G		SPRINTARS-KK
GISS-E2-1-H		UKESM1-A
HadGEM3-GC31-LL		
IPSL-CM5A2-INCA		
IPSL-CM6A-LR-INCA		
KIOST-ESM		
MIROC6		
MIROC-ES2L		
MPI-ESM-1-2-HAM		
MRI-ESM2-0		
NorESM2-LM		
NorESM2-MM		
UKESM1-0-LL		

44 **Supplementary Table 2** Parameters for estimating SW ERF_{aci} from liquid clouds
 45 following the method of Bellouin et al. (2020; hereafter B20). The table includes the
 46 parameter, its notation in B20, the original 66% CI that B20 estimated for the global
 47 mean, and the revised 66% CI that we estimate for the mean over ocean between 55°S
 48 and 55°N.

49

Parameter	Notation in B20	Original 66% CI	Revised 66% CI
present-day aerosol optical thickness	τ_a	0.13 to 0.17	0.11 to 0.15
change in aerosol optical thickness between preindustrial and present day	$\Delta\tau_a$	0.02 to 0.04	0.015 to 0.031
$\frac{\partial R}{\partial \ln N_d}$ (W m ⁻²)	S_N	-27 to -26	-30 to -29
$\frac{\partial R}{\partial \ln LWP}$ (W m ⁻²)	$S_{L,N}^*$	-56 to -54**	-75 to -73**
$\frac{\partial R}{\partial C_{tot}}$ (W m ⁻²)	$S_{C,N}^*$	-153 to -91**	-184 to -111**
$\frac{\partial \ln N_d}{\partial \ln \tau_a}$	$\beta_{\ln N - \ln \tau}$	0.3 to 0.8	0.3 to 0.8
$\frac{d \ln LWP}{d \ln N_d}$	$\beta_{\ln L - \ln N}$	-0.36 to -0.011	-0.36 to -0.011
$\frac{d C_{tot}}{d \ln N_d}$	$\beta_{C - \ln N}$	0 to 0.1	0 to 0.1
effective cloud fraction for Twomey effect	c_N	0.19 to 0.29	0.20 to 0.29
effective cloud fraction for LWP adjustment	c_L	0.21 to 0.29	0.26 to 0.34
effective cloud fraction for cloud-fraction adjustment	c_C	0.59 to 1.07	0.61 to 0.96

50 *These terms represent $S_{L,N}$ and $S_{C,N}$ as defined in equations 19 and 21 of B20.

51
 52 **B20's original assessment of $\partial R / \partial \ln LWP$ and $\partial R / \partial C_{tot}$ represents top-of-atmosphere
 53 net radiation. They assess the SW component of $\partial R / \partial \ln LWP$ and $\partial R / \partial C_{tot}$, then scale
 54 the values by 0.9 to account for an offsetting change in top-of-atmosphere longwave
 55 flux. In our analysis, we estimate the SW component of ERF_{aci}, so we do not apply the
 56 scaling factor of 0.9.

Supplementary Text

Validation of R' Decomposition

Our radiative decomposition method partitions R' into components associated with cloud-amount anomalies, r_e anomalies, LWP anomalies, and a residual:

$$R' = R'_{CF} + R'_{r_e} + R'_{LWP} + R'_{res}.$$

We validate this decomposition using synthetic-data test cases performed with pixel data from the MODIS MYD06_L2 dataset collection 6.1 (Platnick et al., 2015). Each case uses pixels from a $1^\circ \times 1^\circ$ ocean grid box from the entire month of June 2013. Let $r_{e,j}$, LWP_j , and τ_j represent the retrieved cloud properties for a pixel j containing a liquid cloud. For the test cases, we define the original cloud population as the set of all liquid-cloud pixels in the grid box with optical properties given by $r_{e,j}$, LWP_j , and τ_j . We then modify the cloud properties to create a second cloud population, denoted by $\tilde{r}_{e,j}$, \widetilde{LWP}_j , and $\tilde{\tau}_j$, while holding the total number of liquid-cloud pixels constant. The difference in the monthly-mean grid-box-mean SW CRE between the two cloud populations, R' , is then computed. We decompose R' separately using theoretical calculations and the radiative-kernel method, and we compare the estimates for validation.

The first step is to define the modified liquid-cloud population. We define the following relationships between the original and modified clouds:

$$\delta_{r_{e,j}} \equiv \tilde{r}_{e,j} - r_{e,j} = \chi_{r_e} r_{e,j},$$

$$\delta_{LWP,j} \equiv \widetilde{LWP}_j - LWP_j = \begin{cases} \chi_{LWP,1} LWP_j, & r_{e,j} < 14 \mu\text{m} \\ \chi_{LWP,2} LWP_j, & r_{e,j} \geq 14 \mu\text{m}. \end{cases}$$

where δ represents the difference between the original and modified cloud properties and χ_{r_e} , $\chi_{LWP,1}$, and $\chi_{LWP,2}$ are prescribed constants. A piecewise relationship for δLWP_j is chosen because precipitating and non-precipitating clouds can be approximately distinguished based on the clouds that have $r_e \geq 14 \mu\text{m}$ and $r_e < 14 \mu\text{m}$, respectively (Freud and Rosenfeld, 2012; Suzuki et al., 2010). We prescribe separate relationships for precipitating and non-precipitating clouds to mimic the fact that they can have distinct responses to CCN anomalies. Calculations are performed with χ_{r_e} , $\chi_{LWP,1}$, and $\chi_{LWP,2}$ ranging from -0.1 to 0.1 in increments of 0.005 at three grid boxes corresponding to typical midlatitude, stratocumulus, and trade-cumulus conditions (Supplementary Fig. 3a). Each combination of χ_{r_e} , $\chi_{LWP,1}$, $\chi_{LWP,2}$, and grid-box location is referred to as a test case.

We next estimate the difference in liquid-cloud SW CRE between the original and modified cloud populations for each test case under idealized conditions. Assuming that the ocean surface is black, that cloud droplets have a constant asymmetry factor of $g = 0.85$, and neglecting SW absorption by clouds and atmospheric gases, the top-of-atmosphere albedo above each liquid-cloud pixel, α_j , can be estimated using the two-stream radiative transfer approximation (Petty, 2006):

$$\alpha_j = \frac{(1-g)\tau_j}{1+(1-g)\tau_j}.$$

Because $\tau \propto \text{LWP}/r_e$ for this cloud model, the albedo difference between the original and modified cloud populations can be expressed as

$$\delta\alpha_j \equiv \tilde{\alpha}_j - \alpha_j = \delta\alpha_{\text{LWP},j} + \delta\alpha_{r_e,j}$$

where

$$\delta\alpha_{\text{LWP},j} = \frac{\delta\text{LWP}_j}{\text{LWP}_j} \frac{(1-g)\tau_j}{(1+(1-g)\tau_j)^2}$$

and

$$\delta\alpha_{r_e,j} = -\frac{\delta r_{e,j}}{r_{e,j}} \frac{(1-g)\tau_j}{(1+(1-g)\tau_j)^2}.$$

Here, $\delta\alpha_{\text{LWP},j}$ and $\delta\alpha_{r_e,j}$ are the components of $\delta\alpha_j$ that are caused by δLWP_j and $\delta r_{e,j}$, respectively. We next average over all liquid-cloud pixels to determine the components of R' at the monthly-mean grid-box-mean scale:

$$R'_{\text{LWP}} = \text{SW}_\downarrow f_{\text{liq}} \frac{1}{N} \sum_{j=1}^N \delta\alpha_{\text{LWP},j},$$

$$R'_{r_e} = \text{SW}_\downarrow f_{\text{liq}} \frac{1}{N} \sum_{j=1}^N \delta\alpha_{r_e,j},$$

where SW_\downarrow is the monthly-mean insolation; N is the number of liquid-cloud pixels in the grid box; and $f_{\text{liq}} \equiv N/N_{\text{tot}}$, where N_{tot} is the total number of pixels in the grid box. The liquid-cloud fraction is held constant in the test cases, so $R'_{\text{CF}} = 0$.

We next decompose R' using the radiative kernel method. For consistency with the theoretical calculations, the kernel for this analysis is computed with a surface albedo of zero and with no SW absorption by water vapor or ozone. We then bin the liquid-cloud pixels into joint histograms partitioned by r_e and LWP. Let C_{rl} and \tilde{C}_{rl} represent the joint histograms of the original and modified cloud populations, respectively. We define the cloud-fraction anomalies as $C'_{rl} = \tilde{C}_{rl} - C_{rl}$, and we estimate R'_{r_e} , R'_{LWP} , and R'_{res} with the kernel method.

This set of calculations produces estimates of R'_{r_e} for R'_{LWP} from two independent methods for each of the $\sim 2 \times 10^5$ test cases. The theoretical and kernel-based estimates approximately agree across all test cases, and the residual of the kernel decomposition is almost always one order of magnitude smaller than R'_{r_e} and R'_{LWP} .

(Supplementary Fig. 3). This verifies that the kernel method accurately decomposes R' into r_e -driven and LWP-driven components with a relatively small residual.

Assumptions about Cloud Vertical Structure

Cloud visible optical thickness τ and LWP can be expressed as

$$\tau = \int_0^h \frac{3Q_e q_l(z)}{4\rho_l r_e(z)} dz$$

and

$$\text{LWP} = \int_{z=0}^h q_l(z) dz,$$

where z is height above cloud base, h is cloud geometric thickness, $q_l(z)$ is the vertical profile of liquid water content, $r_e(z)$ is the vertical profile of cloud droplet effective radius, ρ_l is liquid-water density, and $Q_e \approx 2$ is the extinction efficiency at visible wavelengths. The MODIS observations can be used to directly infer τ and r_e near cloud top, but they do not constrain the other parameters in these equations. Thus, MODIS infers LWP indirectly by assuming vertical profiles of $q_l(z)$ and $r_e(z)$. Because τ is proportional to the integral of $q_l(z)/r_e(z)$, different profiles of $q_l(z)$ and $r_e(z)$ can be consistent with the observed value of τ . This means that the true LWP can differ from the MODIS estimate if the true profiles of $q_l(z)$ and $r_e(z)$ differ from the assumed profiles. This LWP bias can occur despite the fact that τ is well constrained by the observations.

We investigate the implications of assumptions about cloud vertical structure by considering three idealized cloud profiles. First, case VU assumes that $q_l(z)$ and $r_e(z)$ are vertically uniform inside the cloud. This assumption is made in the operational MODIS retrieval algorithm. Second, case AD assumes that $q_l(z)$ and $r_e(z)$ vary vertically according to the adiabatic cloud model (Brenguier et al., 2000). In this case, cloud droplet number concentration is constant and $q_l(z)$ increases linearly with height. Third, case 2L assumes that the cloud has two vertically uniform layers following the assumptions in the radiative kernel calculations. The top layer has optical thickness $\tau_1 = 3$, LWP denoted by LWP_1 , and effective radius $r_{e,1} = r_{e,\text{top}}$, where $r_{e,\text{top}}$ is the cloud droplet effective radius at cloud top. The bottom layer has optical thickness of $\tau_2 = \tau - \tau_1$, LWP denoted by LWP_2 , and effective radius $r_{e,2} = mr_{e,\text{top}} + b$, where τ is the total cloud optical thickness and m and b are constants.

For all three cases, τ , LWP, and $r_{e,\text{top}}$ can be related to one another with analytic expressions. The VU and AD cases satisfy the following relations:

$$\text{VU case: } \tau = \frac{3Q_e \text{LWP}_{\text{VU}}}{4\rho_l r_{e,\text{top}}}$$

$$\text{AD case: } \tau = \frac{9Q_e \text{LWP}_{\text{AD}}}{10\rho_l r_{e,\text{top}}}$$

178 where LWP_{VU} and LWP_{AD} are the LWP values inferred from the VU and AD
 179 assumptions, respectively (Wood and Hartmann, 2006). The 2L case is represented by
 180 two cloud layers that each satisfy the VU relation:

$$182 \quad \text{2L case: } \tau = \frac{3Q_e}{4\rho_l} \left(\frac{LWP_1}{r_{e,1}} + \frac{LWP_2}{r_{e,2}} \right)$$

183 For a given τ and $r_{e,top}$, the LWP inferred from these assumptions differ from one
 184 another by 17% or less.

185 We next examine how the assumptions about cloud vertical structure affect
 186 estimates of the R' components. Consider two liquid-cloud pixels in which τ and $r_{e,top}$
 187 are known from MODIS observations. Differentiating the above equations leads to the
 188 following relations:
 189

$$190 \quad \text{VU case: } \delta \ln \tau \approx \delta \ln LWP_{VU} - \delta \ln r_{e,top}$$

$$191 \quad \text{AD case: } \delta \ln \tau \approx \delta \ln LWP_{AD} - \delta \ln r_{e,top}$$

$$192 \quad \text{2L case: } \delta \ln \tau \approx \left(\frac{\tau_1}{\tau_1 + \tau_2} \delta \ln LWP_1 + \frac{\tau_2}{\tau_1 + \tau_2} \delta \ln LWP_2 \right) - \left(\frac{\tau_1}{\tau_1 + \tau_2} \delta \ln r_{e,1} + \frac{\tau_2}{\tau_1 + \tau_2} \delta \ln r_{e,2} \right)$$

193 where δ represents the difference between the two pixels. The first and second terms
 194 on the right side of these equations represent the δLWP -driven and $\delta r_{e,top}$ -driven
 195 components of $\delta \ln \tau$, respectively. These components are identical for the VU and AD
 196 cases because LWP_{VU} is directly proportional to LWP_{AD} . The components of $\delta \ln \tau$ from
 197 the VU and AD cases are also similar to those from the 2L case. For instance, if typical
 198 values of $\tau = 10$ and $r_{e,top} = 14 \mu\text{m}$ are assumed and $\delta \ln \tau$ and $\delta \ln r_{e,top}$ are varied
 199 between 0 and 1, then the δLWP -driven and $\delta r_{e,top}$ -driven components of $\delta \ln \tau$ differ by
 200 2% or less between the three cases. This means that different common assumptions
 201 about cloud vertical structure will lead to similar estimates of R'_e and R'_{LWP} .
 202
 203
 204
 205
 206

207 Estimating ERF_{aci} from the Method of Bellouin et al. (2020)

208 We compare our estimates of SW ERF_{aci} from liquid clouds with estimates from
 209 the assessment of the WCRP reported by Bellouin et al. (2020; hereafter B20). B20
 210 assess the components of ERF_{aci} according to
 211

$$212 \quad IRF_{aci} = \frac{\partial R}{\partial \ln N_d} \frac{\partial \ln N_d}{\partial \ln \tau_a} \frac{\Delta \tau_a}{\tau_{a,PD}} c_N,$$

$$213 \quad A_{LWP} = \frac{\partial R}{\partial \ln LWP} \frac{d \ln LWP}{d \ln N_d} \frac{\partial \ln N_d}{\partial \ln \tau_a} \frac{\Delta \tau_a}{\tau_{a,PD}} c_L,$$

214 and

$$A_{CF} = \frac{\partial R}{\partial C_{tot}} \frac{dC_{tot}}{d \ln N_d} \frac{\partial \ln N_d}{\partial \ln \tau_a} \frac{\Delta \tau_a}{\tau_{a,PD}} c_C,$$

215 where τ_a is aerosol optical depth, “PD” represents present day, and Δ represents the
 216 difference between present day and preindustrial conditions. All terms in these
 217 equations are global averages, and c_N , c_L , and c_C are effective cloud fractions that
 218 account for spatial correlations between the other variables. We estimate the
 219 components of ERF_{aci} following the method of B20, but we modify the values so that
 220 they represent averages over our study domain rather than the entire globe. c_N , c_L , c_C ,
 221 $\partial R / \partial \ln N_d$, and $\partial R / \partial \ln LWP$ are computed following B20’s method but restricting the
 222 calculation to ocean grid boxes between 55°S and 55°N. We use B20’s estimates of
 223 $\partial R / \partial C_{tot}$, $\partial \ln N_d / \partial \ln \tau_a$, $d \ln LWP / d \ln N_d$, and $dC_{tot} / d \ln N_d$ because they are
 224 assessed from studies that mostly investigate clouds in oceanic and coastal
 225 environments. One exception is the upper bound of $dC_{tot} / d \ln N_d$, which is assessed
 226 over the entire globe using GCM output. Finally, we scale B20’s estimate of $\tau_{a,PD}$ by a
 227 factor of $\langle \tau_{a,PD} \rangle_{ocean} / \langle \tau_{a,PD} \rangle_{global}$, where $\langle \tau_{a,PD} \rangle_{ocean}$ is the average of $\tau_{a,PD}$ over ocean
 228 between 55°S and 55°N and $\langle \tau_{a,PD} \rangle_{global}$ is the average of $\tau_{a,PD}$ over the entire globe.
 229 Similarly, we scale B20’s estimate of $\Delta \tau_a$ by $\langle \Delta \tau_a \rangle_{ocean} / \langle \Delta \tau_a \rangle_{global}$. These scaling factors
 230 are calculated with data from the Monitoring Atmospheric Composition and Climate
 231 Reanalysis (Benedetti et al., 2009) for consistency with B20. The original and modified
 232 values of all parameters are listed in Supplementary Table 2.

233

234 **Supplementary References**

235 Bellouin, N., et al.: Bounding Global Aerosol Radiative Forcing of Climate Change. *Rev.*
 236 *Geophys.*, 1–45. <https://doi.org/10.1029/2019rg000660>, 2020.

237 Benedetti, A., et al.: Aerosol Analysis and Forecast in the European Centre for Medium-
 238 Range Weather Forecasts Integrated Forecast System: 2. Data Assimilation. *J.*
 239 *Geophys. Res. Atmos.*, 114, D13,205. <https://doi.org/10.1029/2008JD011115>, 2009.

240 Bennartz, R., and Rausch, J.: Global and Regional Estimates of Warm Cloud Droplet
 241 Number Concentration Based on 13 Years of AQUA-MODIS Observations, *Atmos.*
 242 *Chem. Phys.*, 17, 9815– 9836, <https://doi.org/10.5194/acp-17-9815-2017>, 2017.

243 Brenguier, J. L., et al.: Radiative Properties of Boundary Layer Clouds: Droplet Effective
 244 Radius Versus Number Concentration. *J. Atmos. Sci.*, 57(6), 803–821.
 245 [https://doi.org/10.1175/1520-0469\(2000\)057<0803:RPOBLC>2.0.CO;2](https://doi.org/10.1175/1520-0469(2000)057<0803:RPOBLC>2.0.CO;2), 2000.

246 Freud, E., and Rosenfeld, D.: Linear Relation Between Convective Cloud Drop Number
 247 Concentration and Depth for Rain Initiation. *J. Geophys. Res. Atmos.*, 117(2), 1–14,
 248 <https://doi.org/10.1029/2011JD016457>, 2012.

249 Grosvenor, D. P., et al.: Remote Sensing of Droplet Number Concentration in Warm
 250 Clouds: A Review of the Current State of Knowledge and Perspectives. *Rev.*
 251 *Geophys.*, 56(2), 409–453. <https://doi.org/10.1029/2017RG000593>, 2018.

- 252 Gryspeerdt, E., et al.: Surprising Similarities in Model and Observational Aerosol
253 Radiative Forcing Estimates. *Atmos. Chem. Phys.*, 20(1), 613–623.
254 <https://doi.org/10.5194/acp-20-613-2020>, 2020.
- 255 Petty, G. W.: *A First Course in Atmospheric Radiation, Second Edition* Ch. 13 (Sundog
256 Publishing), 2006.
- 257 Platnick, S., et al.: MODIS Atmosphere L2 Cloud Product (06_L2). NASA MODIS
258 Adaptive Processing System, Goddard Space Flight Center, USA:
259 http://dx.doi.org/10.5067/MODIS/MYD06_L2.061, 2015.
- 260 Suzuki, K., Nakajima, T. Y., and Stephens, G. L.: Particle Growth and Drop Collection
261 Efficiency of Warm Clouds as Inferred from Joint CloudSat and MODIS Observations.
262 *J. Atmos. Sci.*, 67(9), 3019–3032. <https://doi.org/10.1175/2010JAS3463.1>, 2010.
- 263 Wilks, D. S.: “The Stippling Shows Statistically Significant Grid Points.” How Research
264 Results are Routinely Overstated and Overinterpreted, and What to Do about It. *Bull.*
265 *Am. Meteorol. Soc.*, 97, 2263–2274, <https://doi.org/10.1175/BAMS-D-15-00267.1>,
266 2016.
- 267 Wood, R., and Hartmann, D. L.: Spatial Variability of Liquid Water Path in Marine Low
268 Cloud: The Importance of Mesoscale Cellular Convection. *J. Clim.*, 19(9), 1748–
269 1764. <https://doi.org/10.1175/JCLI3702.1>, 2006.
- 270 Zhu, Y., Rosenfeld, D., and Li, Z.: Under What Conditions Can We Trust Retrieved
271 Cloud Drop Concentrations in Broken Marine Stratocumulus? *J. Geophys. Res.*
272 *Atmos.*, 123(16), 8754–8767. <https://doi.org/10.1029/2017JD028083>, 2018.